A GRADIENT SCALING METHOD FOR LAPLACE DOMAIN FULL WAVEFORM INVERSION IN ACOUSTIC-ELASTIC COUPLED MEDIA

SEUNG-GOO KANG[1], CHANGSOO SHIN[2], WANSOO HA[3] and JONG KUK HONG[4]

[1] *Division of Polar Earth-System Sciences, Korea Polar Research Institute, KIOST, Incheon 406-840, South Korea.*
[2] *Department of Energy Systems Engineering, Seoul National University, Seoul 151-742, South Korea. css@model.snu.ac.kr*
[3] *Department of Energy Resources Engineering, Pukyong National University, Busan 608-737, South Korea.*
[4] *Division of Polar Earth-System Sciences, Korea Polar Research Institute, KIOST, Incheon 406-840, South Korea.*

(Received July 13, 2015; revised version accepted February 2, 2016)

ABSTRACT

Kang, S.-G., Shin, C., Ha, W. and Hong, J.K., 2016. A gradient scaling method for Laplace domain full waveform inversion in acoustic-elastic coupled media. *Journal of Seismic Exploration*, 25: 199-227.

In 2D full waveform inversions of acoustic-elastic coupled media, wave propagation is described by the acoustic and isotropic elastic wave equations. To consider the irregular topography of the seafloor in full waveform inversions, the interface between the acoustic and elastic media in wave propagation modeling by the finite element method is represented using both square and isosceles triangular elements. However, numerical artifacts are generated near the seafloor, and widespread abnormal gradient directions are generated in the high velocity area in the target model, when the gradient direction is calculated during full waveform inversion in the Laplace domain. This issue generates unsuitable inversion results near the seafloor. We propose a scaling function that minimizes numerical artifacts in the gradient direction for Laplace domain full waveform inversion of acoustic-elastic coupled media. Based on a heuristic approach, we describe a gradient scaling method of Laplace-domain waveform inversion in acoustic-elastic coupled media that can be used to construct more accurate P- and S-wave velocity models of geological targets beneath the seafloor than previous methods. The technique scales the gradient direction using an accumulated gradient that is generated from the accumulated sum of the squares of the conventional gradient with respect

0963-0651/16/$5.00

to depth. This approach is designed to improve the imaging of large anomalies with high-velocity structures and to attenuate artifacts that are related to an irregular seafloor. We perform numerical tests using the synthetic SEG/EAGE salt model and field data. The numerical results demonstrate the validity of Laplace-domain waveform inversions that are calculated with the new scaling method for acoustic-elastic coupled media. The proposed gradient scaling method reduces artifacts more with field data than in the synthetic case. In particular, the abnormal high velocity areas near the seafloor in the inverted P- and S-wave velocity models are effectively removed by the gradient scaling method. We also conduct frequency-domain waveform inversion using the Laplace-domain inversion results as an initial model to confirm the accuracy of the inverted model of field data from our proposed inversion algorithm. The reverse time migration images and synthetic seismograms that were obtained from the field data indicate that this gradient scaling method is a useful tool for building accurate long-wavelength inverted P-and S-wave velocity models of field data from the Laplace domain full waveform inversion.

KEY WORDS: acoustic-elastic coupled media, full waveform inversion, Laplace domain, gradient direction, scaling method.

INTRODUCTION

Several algorithms have been developed to construct velocity models of subsurface structures using seismic data. Mathematicians and geophysicists have proposed refraction-travel-time tomography techniques (Hampson and Russell, 1984; White, 1989; Zhu and McMechan, 1989; Docherty, 1992; Qin et al., 1993; Stefani, 1995; Shtivelman, 1996; Zhang and Toksöz, 1998; Brenders and Pratt, 2007), which apply ray-tracing methods to calculate first arrival times. Reflection travel time tomography can also be applied and allows building a large-scale velocity models to be constructed based on seismic data (Bishop et al., 1985; Chiu and Stewart, 1987; Farra and Madariaga, 1988). However, reflection travel time tomography involves the time-consuming process of identifying and picking continuous events. Migration velocity analysis (Al-Yahya, 1989; Symes and Carazzone, 1991; Jin and Madariaga, 1993; Docherty et al., 1997) and controlled directional reception tomography (Riabinkin, 1957; Riabinkin et al., 1962; Biondi, 1990, 1992) have been proposed to avoid this difficult identifying and picking step. Stereotomography has also been proposed to improve these methods (Billette and Lambaré, 1998).

Full waveform inversion is another method for constructing velocity models using seismic data, and it was initially developed to recover subsurface information in the time domain (Lailly, 1983; Tarantola, 1984; Gauthier et al., 1986; Kolb et al., 1986; Mora, 1987; Bunks et al., 1995; Shipp and Singh, 2002). This work was subsequently extended to the frequency domain to improve the computational efficiency using parallel computation for each frequency (Geller and Hara, 1993; Pratt et al., 1998; Operto et al., 2004; Sirgue and Pratt, 2004; Shin and Min, 2006; Choi et al., 2008; Plessix et al., 2009; Brossier et al., 2009; Sirgue et al., 2009; Vigh et al., 2010). However, frequency-domain full waveform inversion is limited by the requirement to include low-frequency information (Virieux and Operto, 2009).

A Laplace-domain waveform inversion technique has recently been proposed to address the problem of the initial model when performing inversions in the frequency or time domains (Shin and Cha, 2008; Shin and Ha, 2008; Bae et al., 2010; Chung et al., 2010; Ha et al., 2010b; Pyun et al., 2011). Laplace-domain waveform inversion solves the problems of insufficient low-frequency information by using the zero-frequency component of a damped wavefield (Shin and Cha, 2008). By combining the work of Bae et al. (2010) and Kim et al. (2009), Kang et al. (2012) has been developed an inversion algorithm that can account for the effects of elastic waves in marine environments while taking into account irregular submarine topography. However, this algorithm can produce gradient artifacts of Laplace-domain waveform inversion near the seafloor, especially in the case of rough topography in the field data.

In this study, we propose an improved gradient scaling approach for 2D Laplace-domain waveform inversion. The algorithm was developed empirically through several numerical experiments. Our gradient scaling is computed using the sum of the squares of the conventional gradient values that accumulate with depth. This scaling function is designed to enhance the recovery of high-velocity deep-water structures, such as salt domes, while suppressing artifacts that are related to an irregular seafloor. We present inversion examples of synthetic and field data to verify the accuracy of the proposed algorithm. The numerical tests show that the gradient scaling method can diminish the numerical artifacts of the gradient and thus construct more accurate inverted models for acoustic-elastic coupled media than conventional methods. In the case of the field data test, inverted models of the Laplace domain full waveform inversion from the conventional approach result in abnormal high P-wave and S-wave velocity values at the seafloor that are caused by numerical artifacts in the gradient direction. However, the inverted models from the scaled gradient direction method do not contain the abnormal high velocity areas. We evaluate the inversion results of the field data using reverse time migration images and synthetic seismograms that are obtained from the inversion results to verify the inverted models from the scaled gradient method.

WAVE PROPAGATION MODELING FOR ACOUSTIC-ELASTIC COUPLED MEDIA IN THE LAPLACE DOMAIN

By applying the finite element method, we can obtain a discretized matrix equation for acoustic-elastic coupled media with irregular topography. The acoustic and isotropic elastic wave equations with irregular interface conditions can be expressed by the finite element method (Kim et al., 2009):

$$\begin{pmatrix} \mathbf{K}^A + s^2/c^2\,\mathbf{M}^A & \rho_A s^2 \mathbf{Q}^A \sin\theta & \rho_A s^2 \mathbf{Q}^A \cos\theta \\ \left[\mathbf{Q}^E\right]^T \sin\theta & \mathbf{K}^{11} - \rho_E s^2 \mathbf{M}^{11} & \mathbf{K}^{12} \\ \left[\mathbf{Q}^E\right]^T \cos\theta & \mathbf{K}^{21} & \mathbf{K}^{22} - \rho_E s^2 \mathbf{M}^{22} \end{pmatrix} \begin{pmatrix} \tilde{\mathbf{p}}(s) \\ \tilde{\mathbf{h}}(s) \\ \tilde{\mathbf{v}}(s) \end{pmatrix} = \begin{pmatrix} \tilde{\mathbf{f}}(s) \\ 0 \\ 0 \end{pmatrix}, \quad (1)$$

where s is the Laplace damping constant, c is the velocity of the acoustic media, ρ_A is the density of the water column, ρ_E is the density of the elastic media, $\mathbf{K}_A$ is the stiffness matrix for the acoustic media, $\mathbf{K}^{11}$, $\mathbf{K}^{12}$, $\mathbf{K}^{21}$ and $\mathbf{K}^{22}$ are the stiffness matrices for the elastic media, $\mathbf{M}^A$ is the mass matrix for the acoustic media, $\mathbf{M}^{11}$ and $\mathbf{M}^{22}$ are the mass matrices for the elastic media, $\mathbf{Q}^A$ and $\mathbf{Q}^E$ are the interface boundary matrices for the acoustic and elastic media, respectively, θ is the slope of the interface between the acoustic and elastic layers, $\tilde{\mathbf{p}}(s)$ is a pressure-field vector, and $\tilde{\mathbf{h}}(s)$ and $\tilde{\mathbf{v}}(s)$ are the horizontal and vertical displacements of the elastic media in the Laplace domain, respectively (Kim et al., 2009; Kang et al., 2012).

The Laplace-transformed pressure, displacements and source term can be obtained from the time-domain wavefields using the Laplace transform (Bae et al., 2010):

$$\tilde{\mathbf{p}}(s) = \int_0^\infty \mathbf{p}(t) e^{-st} dt \ , \quad (2)$$

$$\tilde{\mathbf{h}}(s) = \int_0^\infty \mathbf{h}(t) e^{-st} dt \ , \quad (3)$$

$$\tilde{\mathbf{v}}(s) = \int_0^\infty \mathbf{v}(t) e^{-st} dt \ , \quad (4)$$

$$\tilde{\mathbf{f}}(s) = \int_0^\infty \mathbf{f}(t) e^{-st} dt \ , \quad (5)$$

We can simplify eq. (1) using the impedance matrix $\mathbf{S}$:

$$\mathbf{S}\tilde{\mathbf{u}} = \tilde{\mathbf{f}} \ , \quad (6)$$

where $\tilde{\mathbf{u}}$ is the Laplace-domain wavefield vector that contains the pressure field and the displacements.

WAVEFORM INVERSION USING A SCALED GRADIENT

Here, we describe our inversion algorithm that uses a new gradient scaling method for acoustic-elastic coupled media. We use the Lamé parameters $\lambda(x,z)$ and $\mu(x,z)$ and the density $\rho_E(x,z)$ as the elastic model parameters for the waveform inversion. After the inversion results are obtained using the Lamé parameters, the models of the Lamé parameters are converted into P-wave velocity, S-wave velocity and density values (Choi et al., 2008; Kim et al., 2009; Bea et al., 2010; Kang et al., 2012).

Unlike the wavefield in frequency-domain full waveform inversion, the Laplace-domain wavefield exhibits small values because the Laplace-domain full waveform inversion uses the damped wavefield (Shin and Cha, 2008). Given these conditions, the logarithmic objective function (Shin and Min, 2006) is more useful than the conventional l_2 objective function for measuring residuals (Shin and Cha, 2008; Shin and Ha, 2008). Numerous studies associated with Laplace-domain waveform inversions have obtained successful results using the logarithmic objective function (Shin and Cha, 2008; Bae et al., 2010; Chung et al., 2010; Ha et al., 2010a; Pyun et al., 2011). The logarithmic objective function for our Laplace-domain waveform inversion method for a given Laplace damping constant is expressed by (Shin and Min, 2006; Shin and Cha, 2008):

$$G(k_{(x,z)}) = \tfrac{1}{2} \sum_{i=1}^{n_s} \sum_{j=1}^{n_r} \delta\tilde{r}_{ij}\delta\tilde{r}_{ij} \quad , \tag{7}$$

$$\delta\tilde{r}_{ij} = \ln(\tilde{u}_{ij}/\tilde{d}_{ij}) \quad , \tag{8}$$

where $\tilde{d}_{ij}$, $\tilde{u}_{ij}$ and $\delta\tilde{r}_{ij}$ are the observed wavefield, modeled wavefield, and residual at the j-th receiver by the i-th source, respectively, and n_s and n_r are the total numbers of sources and receivers, respectively. Using the back-propagation algorithm, we can effectively calculate the gradient of the objective function with respect to the model parameter $k_{(x,z)}$ by (Tarantola, 1984; Pratt et al., 1998):

$$\nabla_{k_{(x,z)}} \mathbf{G}(x,z) = \mathrm{Re}\left[\sum_{i=1}^{n_s} (\mathbf{vf}_{k_{(x,z)}})^T \mathbf{S}^{-1} \delta\tilde{\mathbf{r}}_i \right] \quad , \tag{9}$$

where $\mathbf{vf}_{k_{(x,z)}}$ is the virtual source term, which is defined as:

$$\mathbf{vf}_{k_{(x,z)}} = -(\partial\mathbf{S}/\partial k_{(x,z)})\tilde{\mathbf{u}}_i \quad , \tag{10}$$

where $\tilde{\mathbf{u}}_i$ is the forward modeled wavefield, and $\delta\tilde{\mathbf{r}}_i$ is the residual for the i-th source, which is defined as:

$$\delta\tilde{\mathbf{r}}_i = \begin{bmatrix} \ln(\tilde{u}_{i1}/\tilde{d}_{i1})/u_{i1} \\ \ln(\tilde{u}_{i2}/\tilde{d}_{i2})/u_{i2} \\ \vdots \\ \ln(\tilde{u}_{i,nr}/\tilde{d}_{i,nr})/u_{i,nr} \\ 0 \\ \vdots \\ 0 \end{bmatrix} . \tag{11}$$

The gradient direction is constructed from the back-propagation algorithm. However, the gradient direction of the conventional full waveform inversion for acoustic-elastic coupled media contains numerical artifacts at the seafloor, which degrade the inversion results.

We propose a gradient scaling algorithm to resolve the numerical artifacts by modifying the conventional gradient using an accumulated gradient, which is calculated using the vertically accumulated sum of the squares of the original gradient values.

The accumulated gradient can be calculated as:

$$\begin{aligned} \nabla_{k_{(x,z)}} \mathbf{G}_{acc}(x,0) &= [\mathrm{Re}[\sum_{i=1}^{n_s} (\mathbf{vf}_{k_{(x,0)}})^T \mathbf{S}^{-1} \delta\tilde{\mathbf{r}}_i]]^2 \\ &= [\nabla_{k_{(x,z)}} \mathbf{G}(x,0)]^2 \quad . \quad x_{min} \le x \le x_{max} \end{aligned} \tag{12}$$

Eq. (12) presents the accumulated gradient of the conventional gradient within the first horizontal layer ($z = 0$). We then sequentially obtain the accumulated gradient:

$$\nabla_{k_{(x,z)}} \mathbf{G}_{acc}(x,z) = \nabla_{k_{(x,z)}} \mathbf{G}_{acc}(x,z-\Delta z) - [\nabla_{k_{(x,z)}} \mathbf{G}(x,z)]^2 \quad . \tag{13}$$

$$x_{min} \le x \le x_{max}, \quad z = 0,\Delta z,\cdots,z_{max}$$

After obtaining the accumulated gradient $\nabla_{k_{(x,z)}} \mathbf{G}_{acc}(x,z)$, we compute the scaled gradient direction $\nabla_{k_{(x,z)}} \mathbf{G}_L(x,z)$ by multiplying the conventional gradient by the accumulated gradient (Code 1):

$$\nabla_{k_{(x,z)}} \mathbf{G}_L(x,z) = [\nabla_{k_{(x,z)}} \mathbf{G}(x,z) \cdot \nabla_{k_{(x,z)}} \mathbf{G}_{acc}(x,z)] \quad . \tag{14}$$

Note that the accumulated gradient is always positive and that the resultant gradient vector is a rescaled gradient. The accumulated gradient tends to focus on large anomalies while minimizing the numerical artifacts on the seafloor. To normalize the gradient, we adopt the diagonal elements of the pseudo-Hessian matrix (Shin et al., 2001).

Code 1. The gradient scaling procedure written in Fortran 90 [eqs. (12), (13) and (14)].

```
accumulated_gradient(1:nx,1) = gradient(1:nx,1)**2
do z=2,nz
  accumulated_gradient(1:nx,z) = accumulated_gradient(1:nx,z-1) + gradient(1:nx,z)**2
enddo
scaled_gradient(1:nx,1:nz) = gradient(1:nx,1:nz) * accumulated_gradient(1:nx,1:nz)
```

After calculating the scaled gradient direction of the objective function, we update the model parameters (Shin and Cha, 2008) as follows:

$$k^{l+1}_{(x,z)} = k^{l}_{(x,z)} - \alpha^{l} \sum_{s=1}^{nf} \mathrm{NRM}[\nabla_{k_{(x,z)}} \mathbf{G}_{L}(x,z) / \{ \sum_{s=1}^{n_s} \mathrm{Diag}[(\mathbf{vf}_{k_{(x,z)}})^{T} \cdot \mathbf{vf}_{k_{(x,z)}}] + \eta \}], \quad (15)$$

where l is the iteration number, α^{l} is the step length in the l-th iteration, nf is the total number of Laplace damping constants, NRM is a normalizing operator (Ha et al., 2009), and η is a stabilizing factor. We estimate the unknown source wavelet from the initial source using the Newton method (Shin et al., 2007). We repeat this procedure iteratively until a stopping criterion is met.

EXPERIMENT USING SYNTHETIC DATA

We first examine the scaled gradient by comparing it to the conventional gradient direction of the modified SEG/EAGE salt model (Aminzadeh et al., 1994). Fig. 1 shows a modified SEG/EAGE salt model (P-wave, S-wave and density) that includes a seawater layer and an irregular seafloor. We modeled wave propagation in acoustic-elastic coupled media based on 2D profile AA' of the SEG/EAGE salt model to generate the recorded data. The data contain 151 shots, each of which has 760 receivers. The shot interval is 100 m, and the receiver interval is 20 m. For the inversions, we use 15 damping constants that range between 1 and 15. The velocities and density of the starting models increase linearly with depth (Fig. 2): the P-wave velocities vary from 1.5 to 3.6 km/s, the S-wave velocities vary from 1.0 to 2.3 km/s, and the densities vary from 1.8 to 2.5 g/cc. The P-wave velocity, S-wave velocity and density of the water layer are 1.5 km/s, 0 km/s and 1 g/cc, respectively.

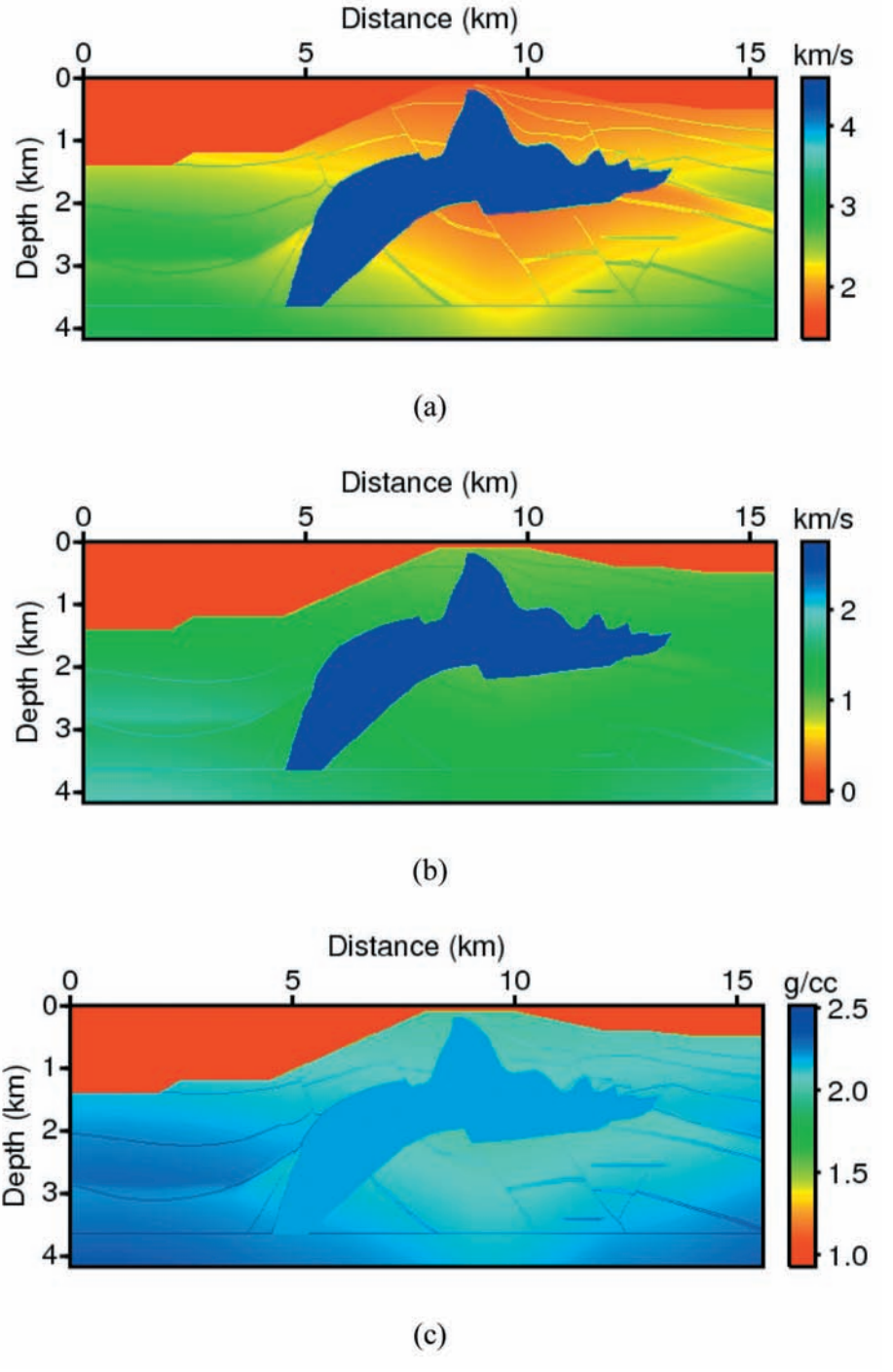

Fig. 1. Modified 2D profile AA' of the SEG/EAGE salt model. (a) P-wave velocity, (b) S-wave velocity, and (c) density.

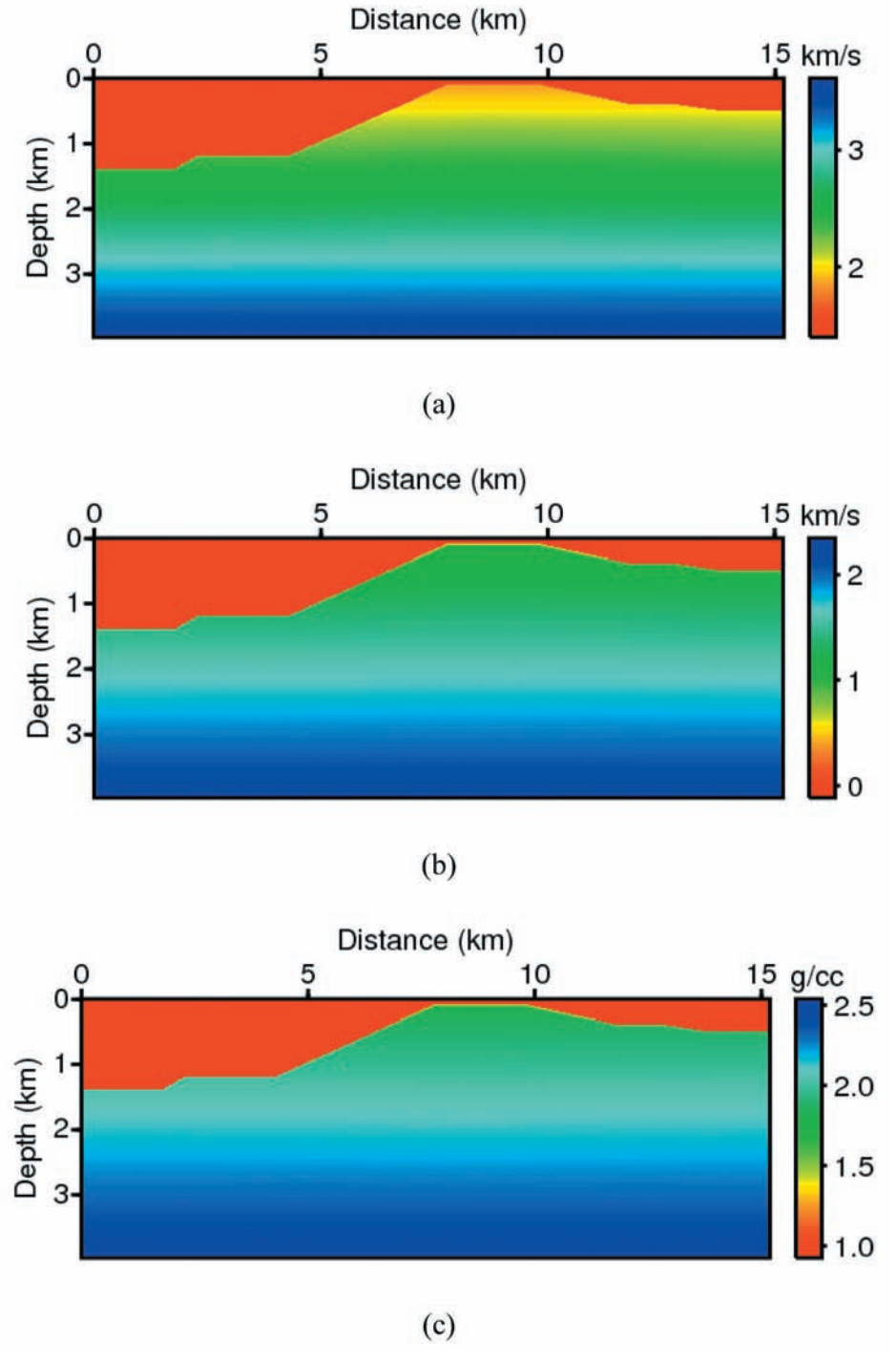

Fig. 2. Starting velocity models for the waveform inversion of the SEG/EAGE salt model. (a) P-wave velocity, (b) S-wave velocity, and (c) density.

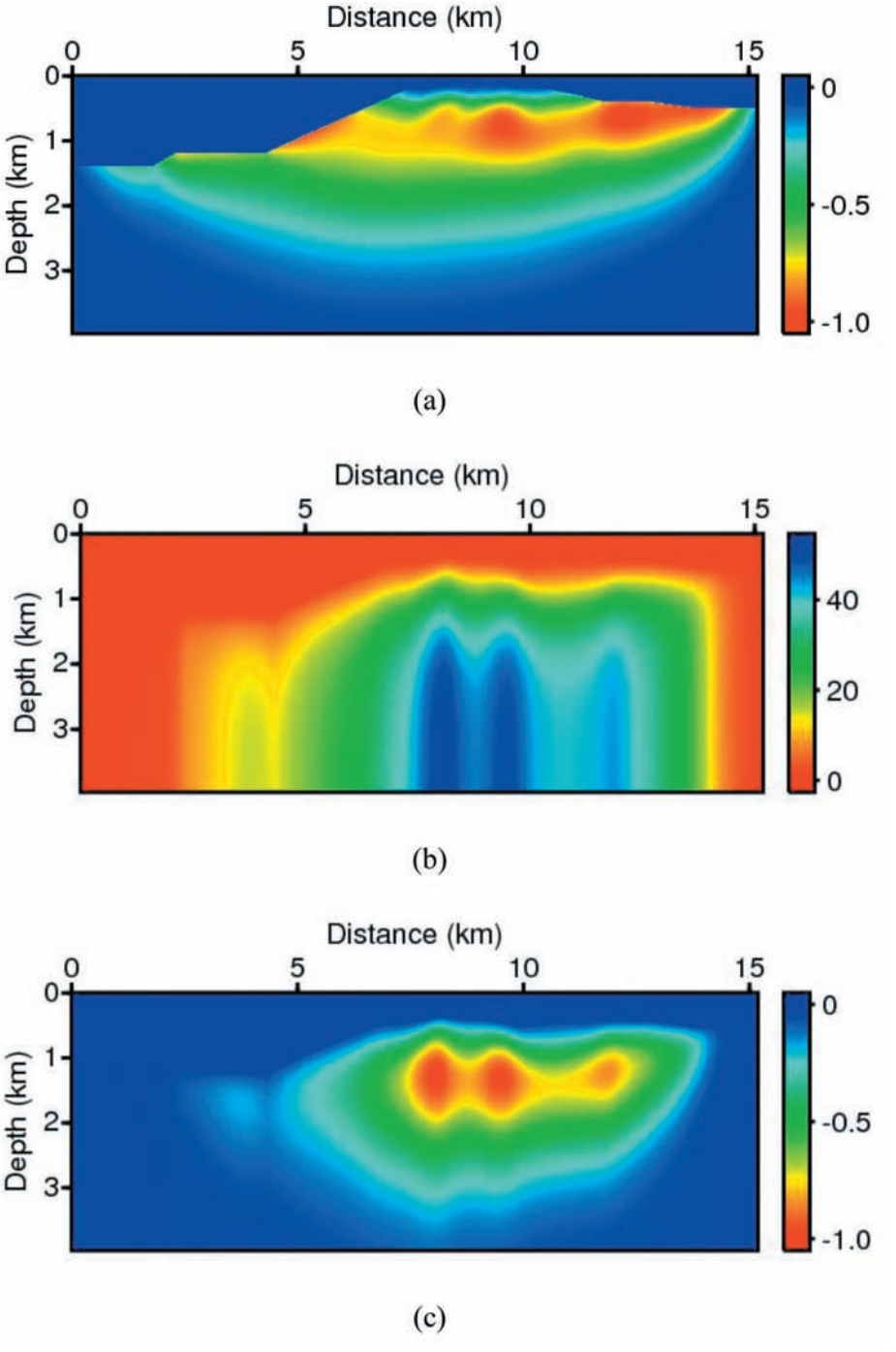

Fig. 3. Calculated gradient directions of the SEG/EAGE salt model for the Laplace domain full waveform inversion. (a) Conventional gradient, (b) accumulated sum of the squares of the conventional gradient, and (c) scaled gradients for $\lambda(x,z)$.

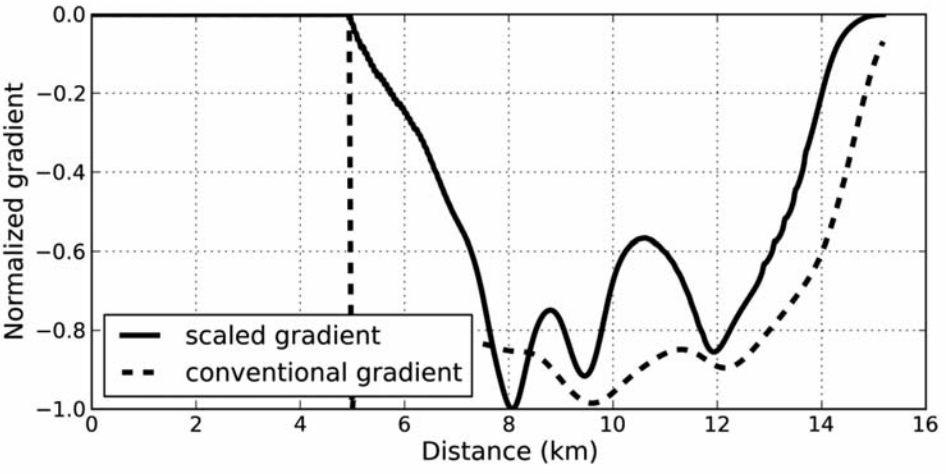

Fig. 4. Horizontal profiles of the conventional and scaled gradient directions for at a depth of 2.5 km.

Fig. 3 shows the conventional, accumulated and scaled gradient directions of $\lambda(x,z)$ in the first iteration. The scaled gradient (Fig. 3c) is computed by multiplying the conventional and accumulated gradients (Figs. 3a and 3b, respectively). The gradient direction of $\mu(x,z)$ behaves similarly to that of $\lambda(x,z)$. The scaled gradient direction concentrates on the high-velocity salt structure and reduces artifacts near the interface. Fig. 4 shows horizontal profiles of the conventional (Fig. 3a) and scaled gradients (Fig. 3c) at a depth of 2.5 km. In the true models in Fig. 1, salt dome structures are located 8 km from the left edge of the model. In Fig. 4, the scaled Laplace gradient (solid black line) is highest at the salt body. However, the conventional gradient direction (dotted black line) cannot detect the exact position of the salt dome in the first iteration. This example shows that the scaled gradient can identify high-velocity zones more accurately than the conventional gradient direction can. Additionally, artifacts near the seafloor are minimized because the accumulated gradient tends to put less weight near the seafloor than on deeper structures.

We invert for the P- and S-wave velocities and density simultaneously within the Laplace domain. However, the density model cannot be recovered fully because the waveform inversion is not sufficiently sensitive to density (Virieux and Operto, 2009). We use 15 damping constants that range between 1 and 15. Fig. 5 shows the inversion results after 100 iterations that were derived from the conventional gradient (Bae et al., 2010), and Fig. 6 shows the inversion results that were derived from the scaled gradient direction. The inversion that was calculated from the scaled gradient direction is superior to that from the conventional method. In Fig. 5, abnormal high velocities were calculated by conventional gradient approach (dotted black rectangular boxes).

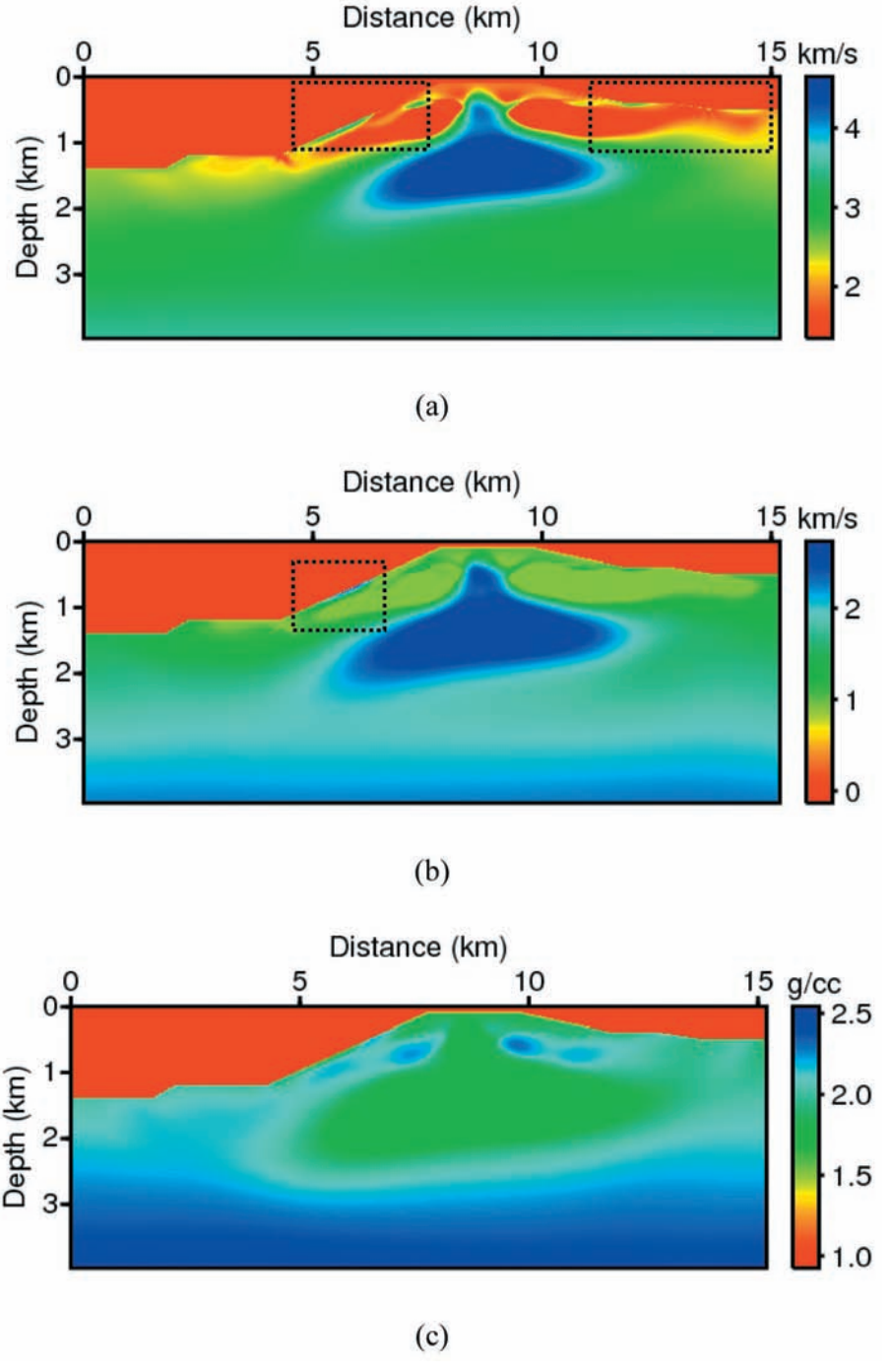

Fig. 5. Results of the Laplace-domain waveform inversion of the SEG/EAGE salt model for acoustic-elastic coupled media using the conventional gradient: (a) inverted P-wave velocity, (b) S-wave velocity, and (c) density models.

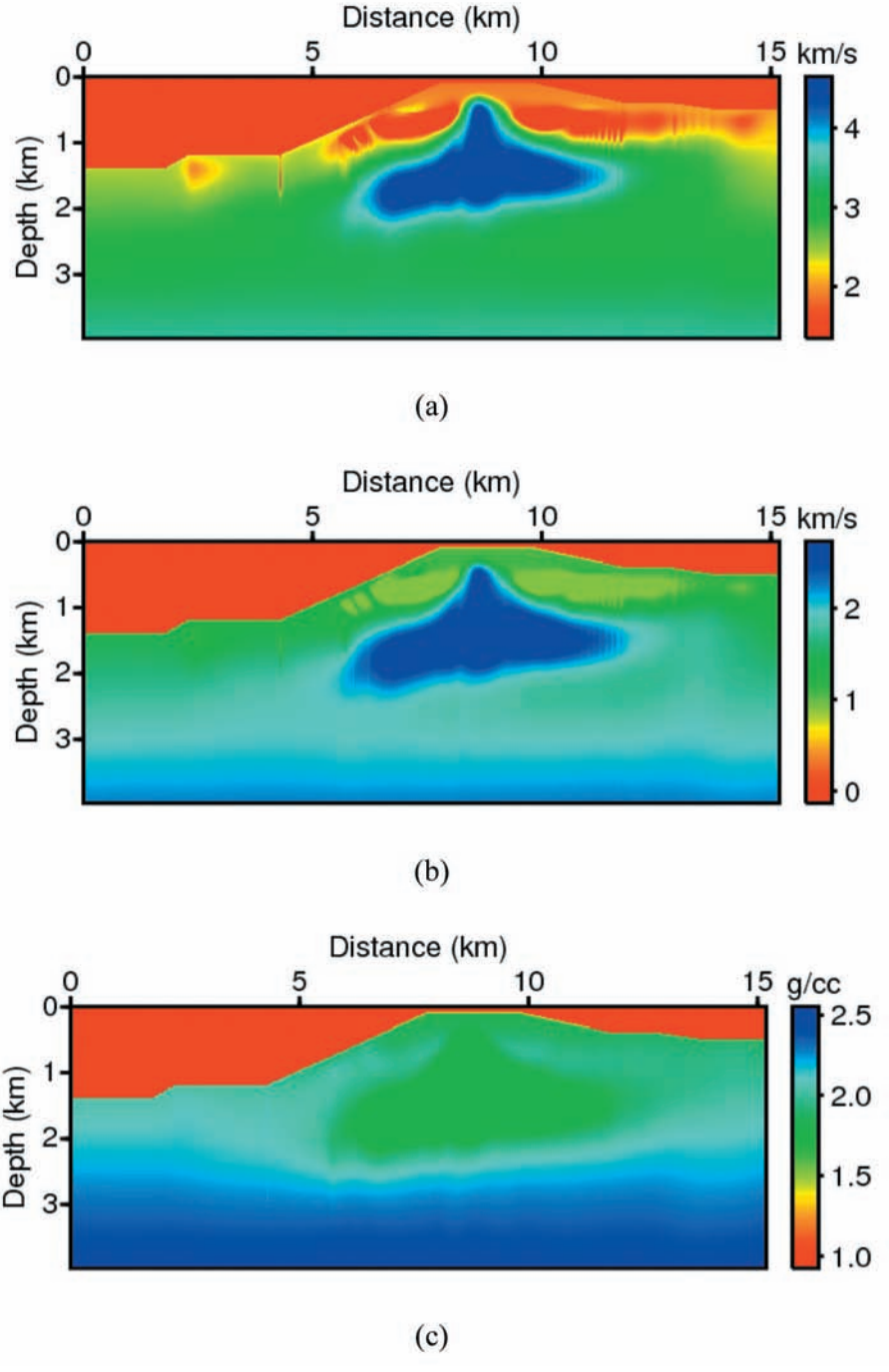

Fig. 6. Results of the Laplace-domain waveform inversion of the SEG/EAGE salt model for acoustic-elastic coupled media using the scaled gradient: (a) inverted P-wave velocity, (b) S-wave velocity, and (c) density models.

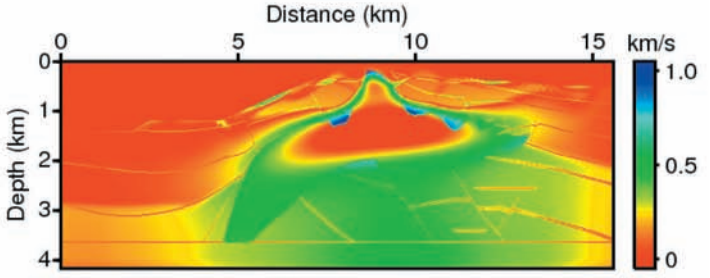

(a)

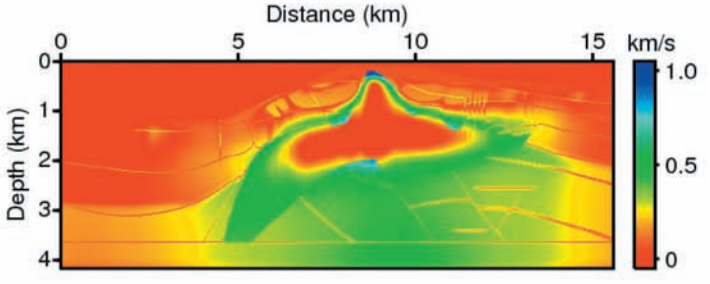

(b)

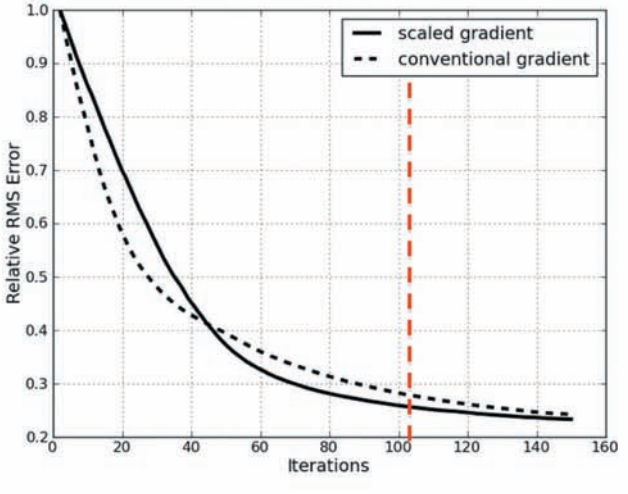

(c)

Fig. 7. Differences between the true P-wave velocity model and the inversion results from (a) the conventional inversion and (b) the inversion using the scaled gradient. (c) Root mean square (RMS) error histories of the two inversion experiments.

However, the inverted velocity models from gradient scaling method (Fig. 6) do not include the abnormal inverted values near the seafloor. The shapes of the salt dome in Fig. 6 are obtained from the scaled gradient direction, and these shapes more closely mimic the true model than those of the conventional algorithm (Fig. 5). Fig. 7a and 7b show the difference between the true velocity models and the inversion results. The results of the conventional algorithm contain high-velocity artifacts near the seafloor (Fig. 7a). However, the inverted models that apply the scaled gradient provide similar results to those of the true models near the interface (Fig. 7b). Fig. 7c shows the error histories of the two inversion cases, which show that the inversion that applies the scaled gradient converges to a smaller error value than the conventional inversion.

EXPERIMENT USING FIELD DATA

After completing the synthetic data test, we applied our inversion algorithm to marine field data (Fig. 8). We applied low-cut filtering to the data and muted the noise prior to the first arrival (Ha and Shin, 2012). The data consist of 1,156 shots, each of which has 804 receivers. The shot interval is 37.5 m, and the receiver interval is 12.5 m. The maximum offset is 10.2 km, and the recording time is 15.0 s. Fig. 8 shows a shot gather from the data.

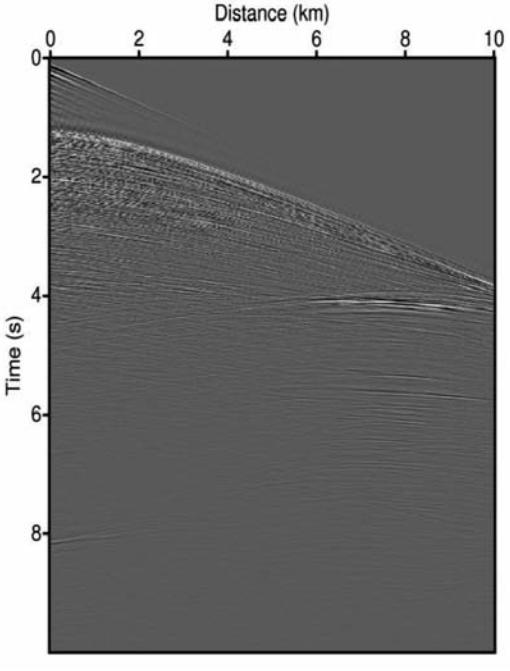

Fig. 8. A shot gather (751st/1156) from the field data after preprocessing (e.g., band-pass filtering, noise muting) for the full waveform inversion test.

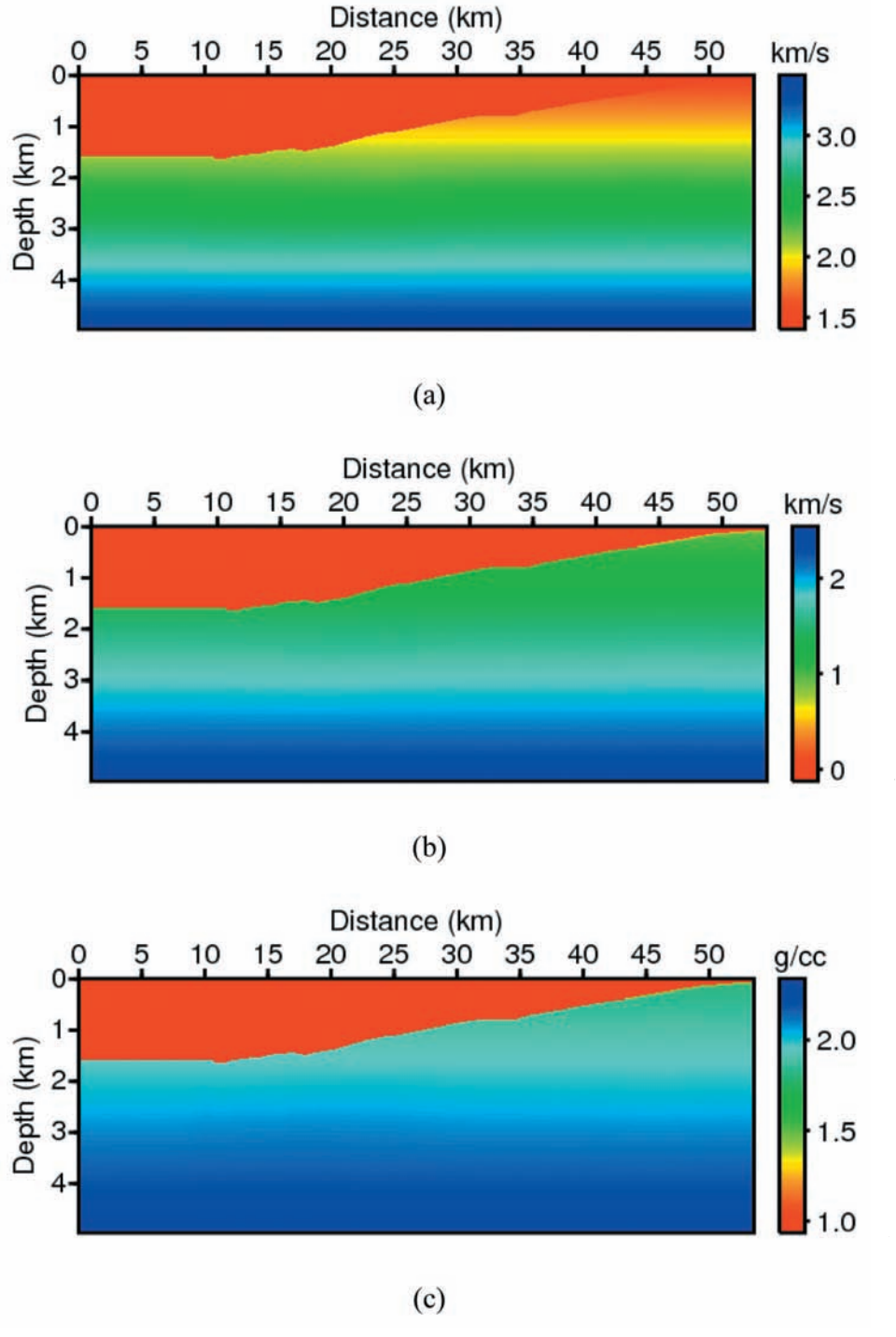

Fig. 9. Starting models for the Laplace-domain waveform inversion of the field data: (a) P-wave velocity, (b) S-wave velocity, and (c) density models.

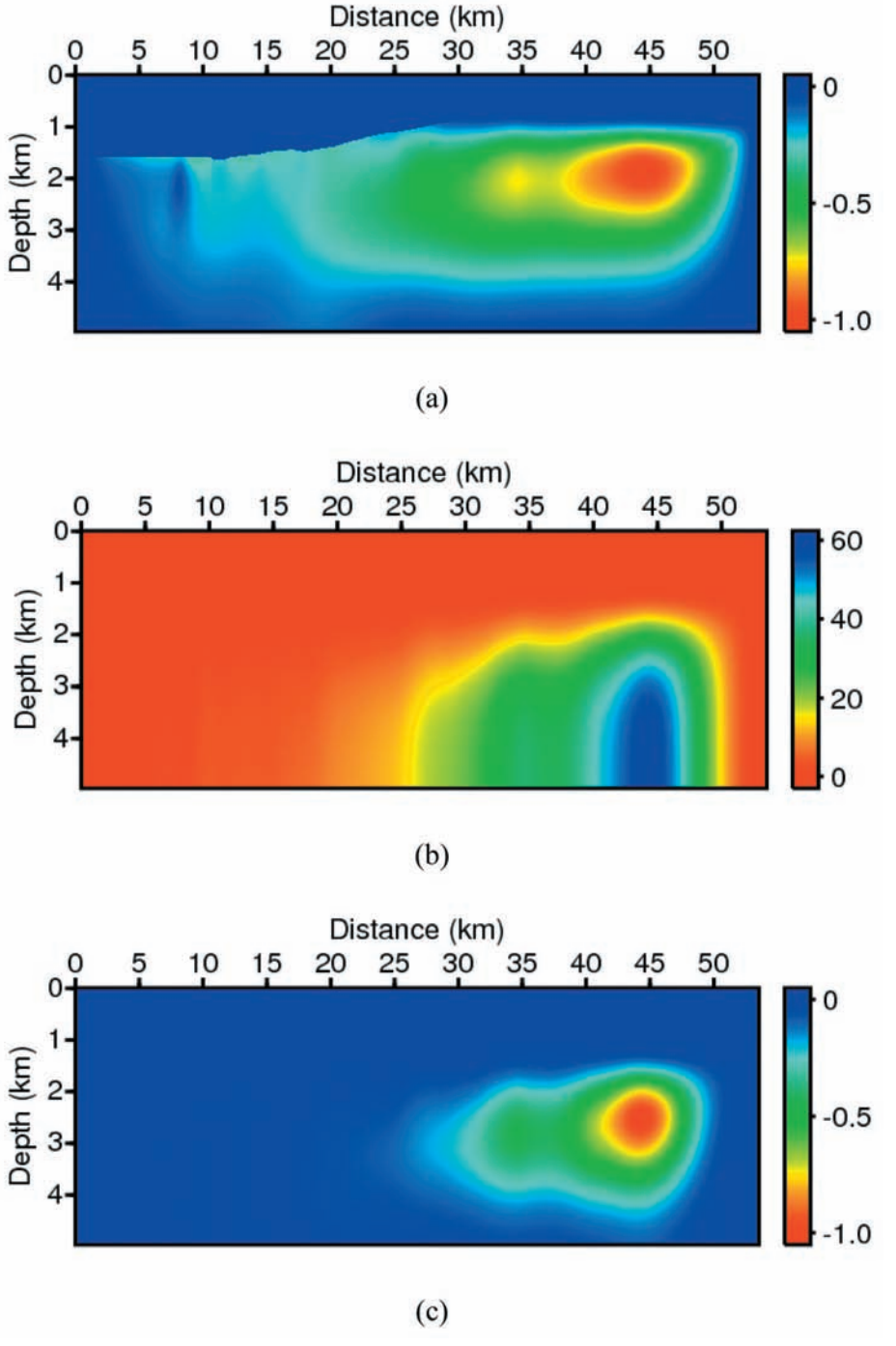

Fig. 10. Calculated gradient directions of the field data for the Laplace domain full waveform inversion. (a) Conventional gradient, (b) accumulated sum of the squares of the conventional gradient, and (c) scaled gradients for $\lambda(x,z)$.

Fig. 9 shows the initial P-wave velocity, S-wave velocity and density models for the field data test. The P-wave velocities increase linearly from 1.5 to 3.5 km/s, the S-wave velocities increase from 0.9 to 2.5 km/s, and the densities vary between 1.8 and 2.3 g/cc. We fixed the P- and S-wave velocities of the water layer at 1.5 km/s and 0 km/s, respectively. The density of the water layer is 1.0 g/cc. We used 10 Laplace damping constants that range from 1 to 10. The inversion grid size was 25 m. Fig. 10 shows the conventional gradient, accumulated gradient and scaled gradient directions; the latter was computed by multiplying the conventional gradient by the accumulated gradient. Fig. 11 shows the horizontal profiles of the conventional and scaled gradients at a depth of 2.5 km, which show that the scaled gradient direction recovers high-velocity anomalies, such as salt dome structures, more effectively than the conventional gradient. Figs. 12 and 13 show the Laplace-domain inversion results after 100 iterations that were derived from the conventional and scaled gradient directions, respectively. Note that the results of the conventional method show the presence of high-velocity artifacts (marking with dotted black rectangular boxes) below the seafloor near the left edge of the model. The artifacts are substantially reduced when the scaling method is applied.

We performed frequency-domain full waveform inversions using the Laplace-domain inversion results as the initial model to examine the accuracy of the results. We used the l_2 objective function with a frequency range of 3.1 to 10.0 Hz. Figs. 14 and 15 show the frequency-domain inversion results after 400 iterations based on the Laplace-domain inversion results that apply the conventional or scaled gradients, respectively. Note that the frequency-domain

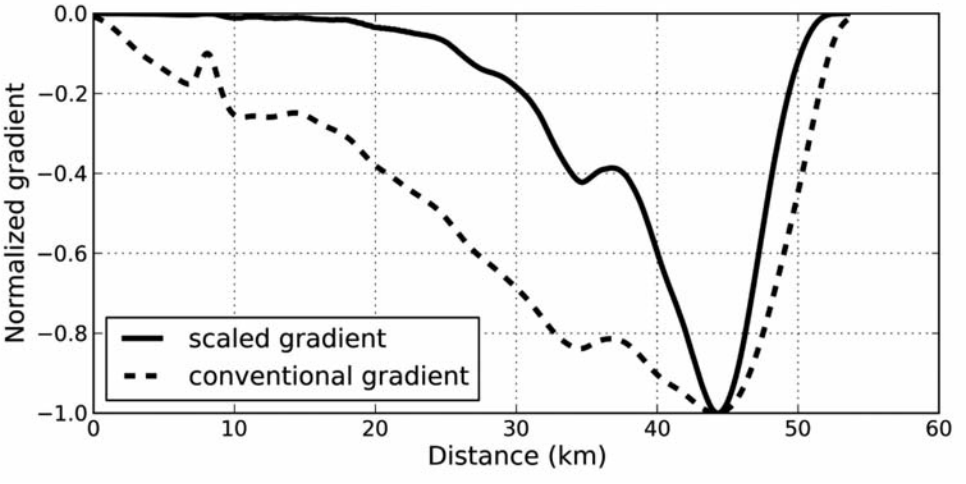

Fig. 11. Horizontal profiles of the conventional and scaled gradient directions for λ(x,z) at a depth of 2.5 km.

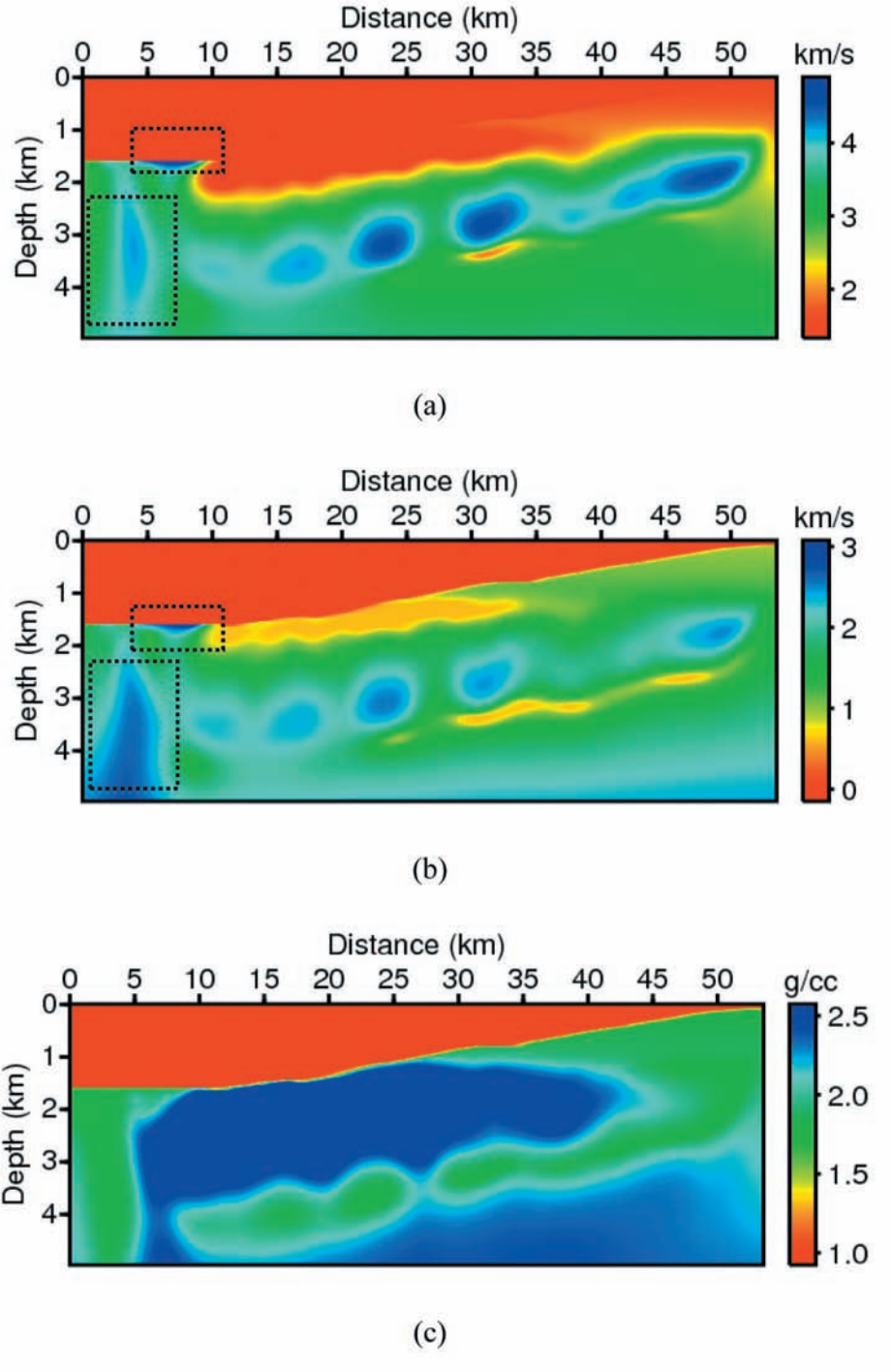

Fig. 12. Results of the conventional Laplace-domain waveform inversion for acoustic-elastic coupled media: (a) inverted P-wave velocity, (b) S-wave velocity, and (c) density models.

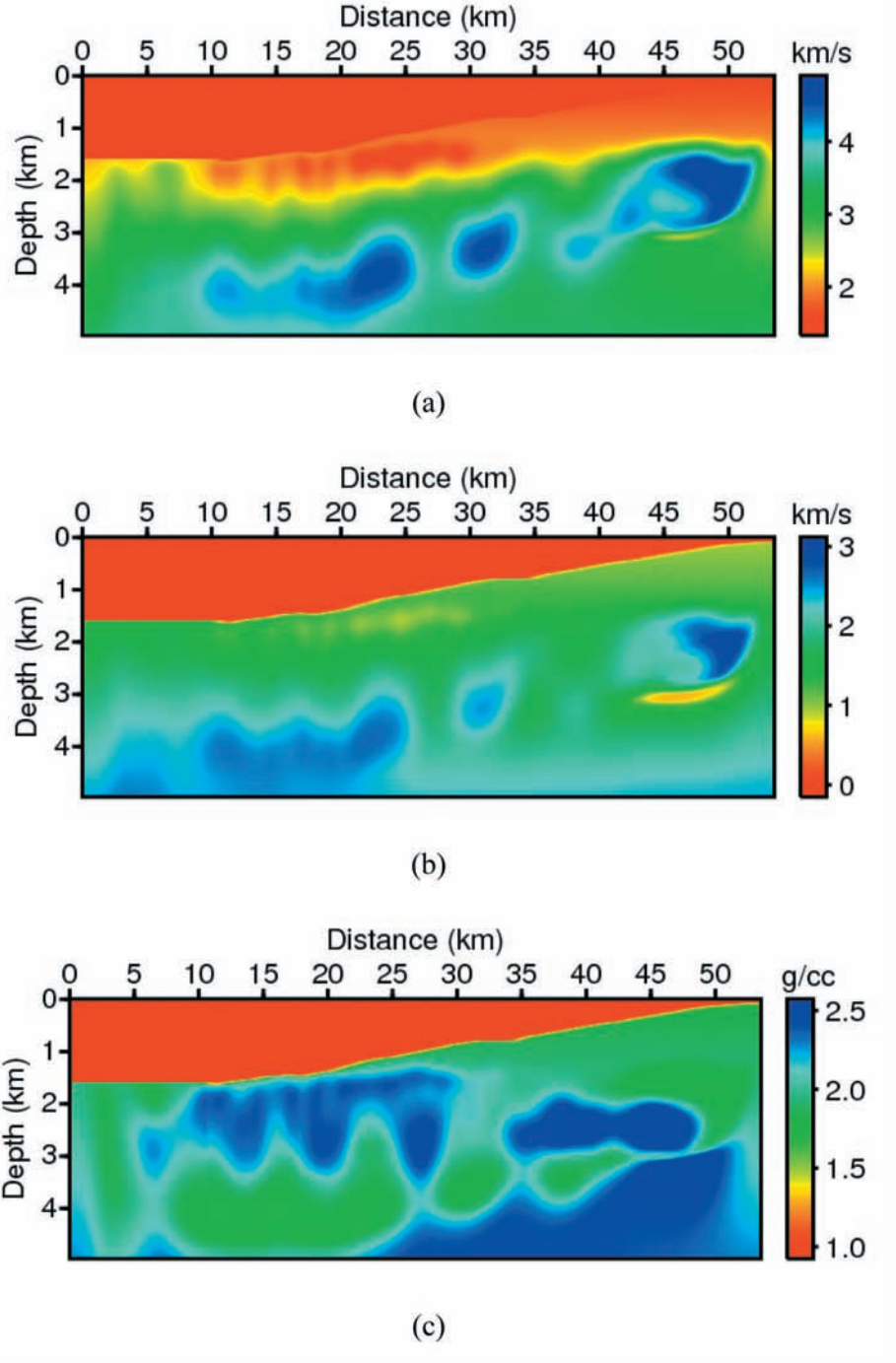

Fig. 13. Results of the Laplace-domain waveform inversion using the scaled gradient for acoustic-elastic coupled media: (a) inverted P-wave velocity, (b) S-wave velocity, and (c) density models.

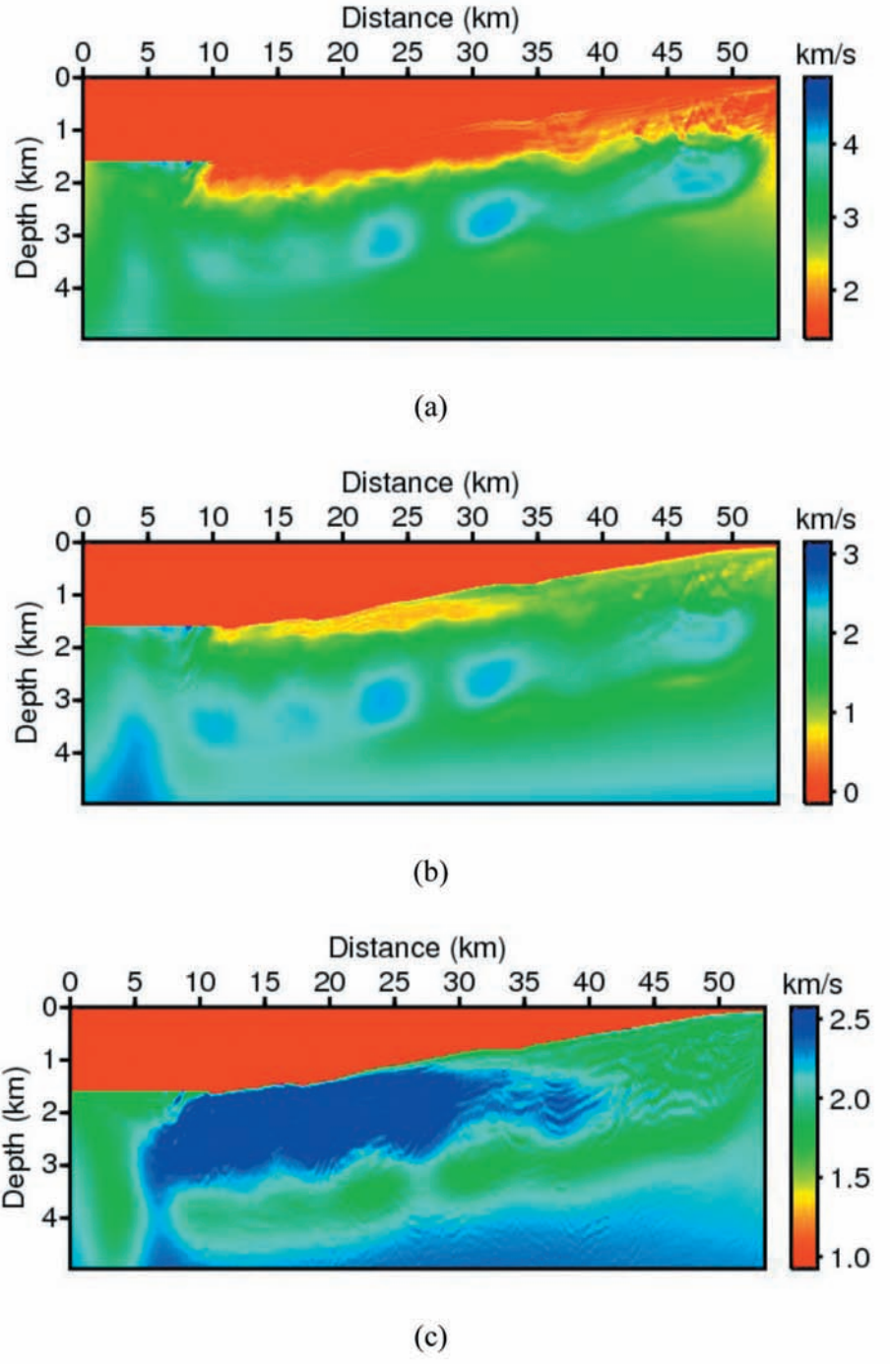

Fig. 14. Results of the frequency-domain waveform inversion for acoustic-elastic coupled media that were obtained using the conventional Laplace-domain inversion results as the initial model: (a) inverted P-wave velocity, (b) S-wave velocity, and (c) density models.

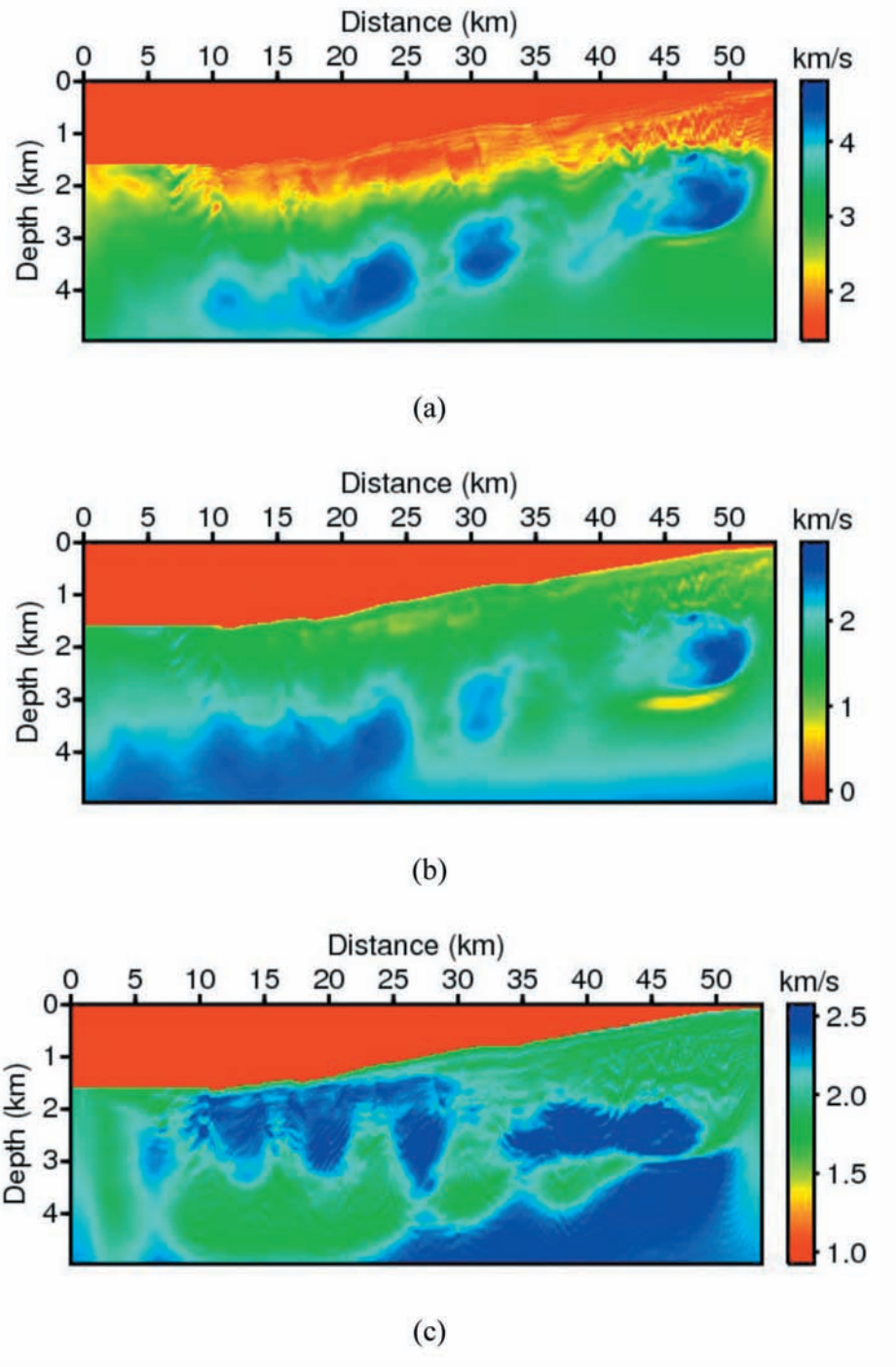

Fig. 15. Results of the frequency-domain waveform inversion for acoustic-elastic coupled media that were obtained using the Laplace-domain inversion results with the scaled gradient direction as the initial model: (a) inverted P-wave velocity, (b) S-wave velocity, and (c) density models.

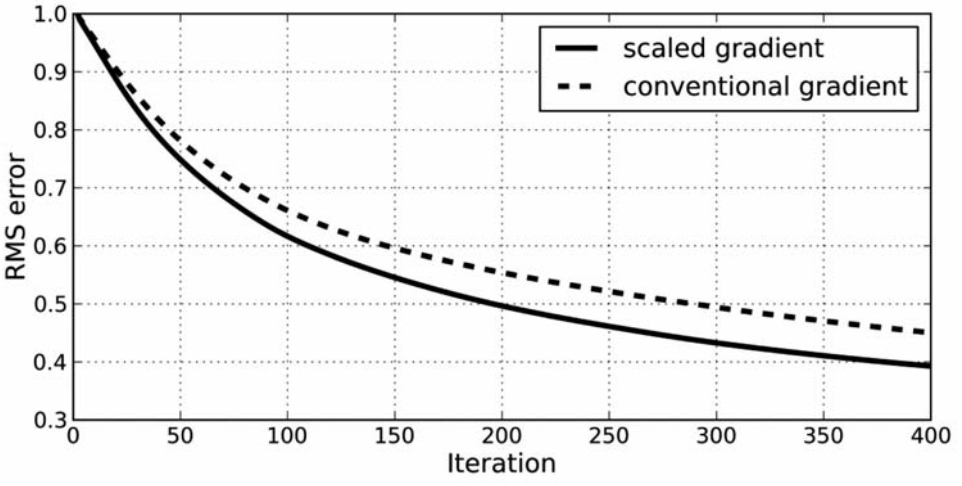

Fig. 16. Error histories of the frequency-domain full waveform inversion using the Laplace-domain inversion results with the conventional and scaled gradient directions.

inversion that applies the Laplace-domain waveform inversion results through the scaled gradient exhibits superior results. In particular, the high-velocity structures in the center are well defined. Fig. 16 shows the error histories of the frequency-domain inversions. Although we inverted the data using the same conditions for both cases, the inversion that used the initial models that were generated from the scaled gradient exhibits superior convergence results.

Fig. 17 shows reverse time migration sections for each inverted model. The acoustic time-domain reverse time sections were generated using the P-wave velocities and a grid size of 20 m. Note that the scaled gradient inversion recovered the high-velocity structures within the velocity model better. A substantial number of events are more coherent in the image that was obtained from the scaling method than in the image that was obtained from the conventional method. Fig. 18 shows common image gathers of the migration algorithm that were extracted at 10 and 26 km as indicated in the migration images (Fig. 17). Although the differences between the results of the common image gathers are not large, the flatness of the gather is improved with the gradient scaling method.

We also generated synthetic seismograms from the inversion results. The seismograms were generated within the frequency domain using frequencies of up to 15 Hz, after which they were transformed into the time domain. We then bandpass-filtered the observed data to match the data frequency contents to the

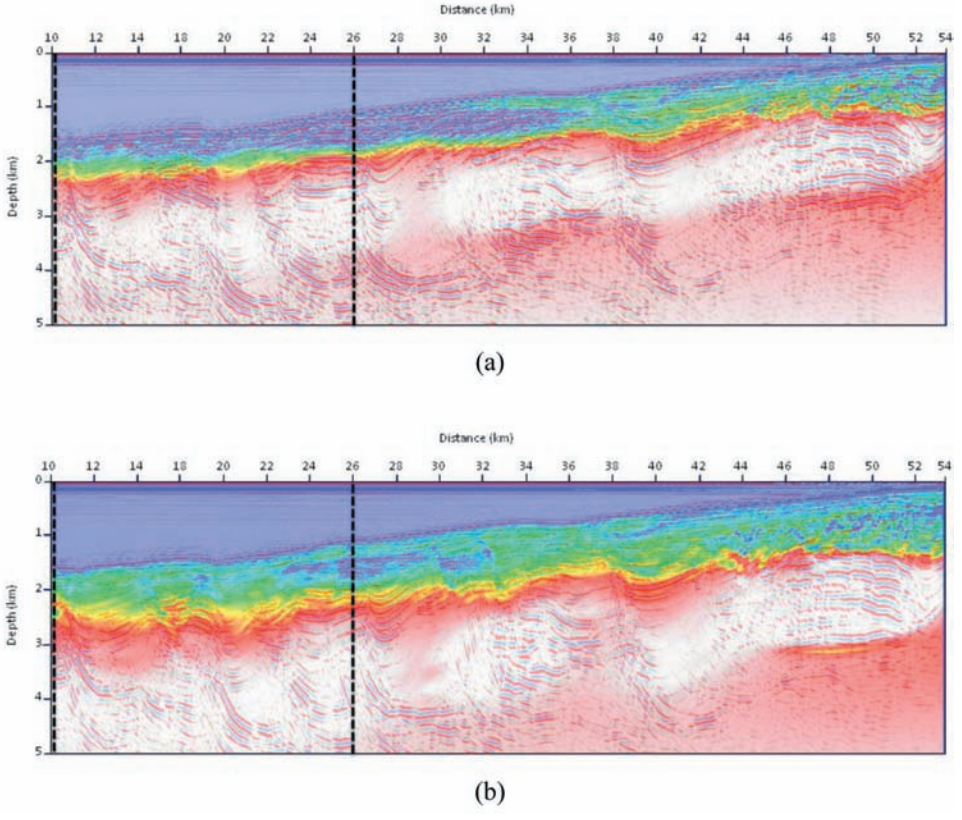

Fig. 17. Reverse time migration sections from the inverted models. The migration images used the inversion results that were obtained from (a) the conventional gradient direction and (b) the scaled gradient direction.

seismograms that were obtained from the inversion. Fig. 19 shows the 751st shot from the observed data and the results of the two inversions. Fig. 19a shows the seismogram that was extracted from the field data, and Figs. 19b and 19c show synthetic seismograms that were generated from the inversion results using the conventional and scaled gradients, respectively. We extracted time traces from the seismograms at an offset of 1.6 km to provide a comparison (Fig. 20). The seismogram that was derived from the scaled gradient results more closely resembles the field trace. Figs. 17 through 20 show that inverting field data using scaled gradients can enhance the recovery of deep-water, high-velocity structures.

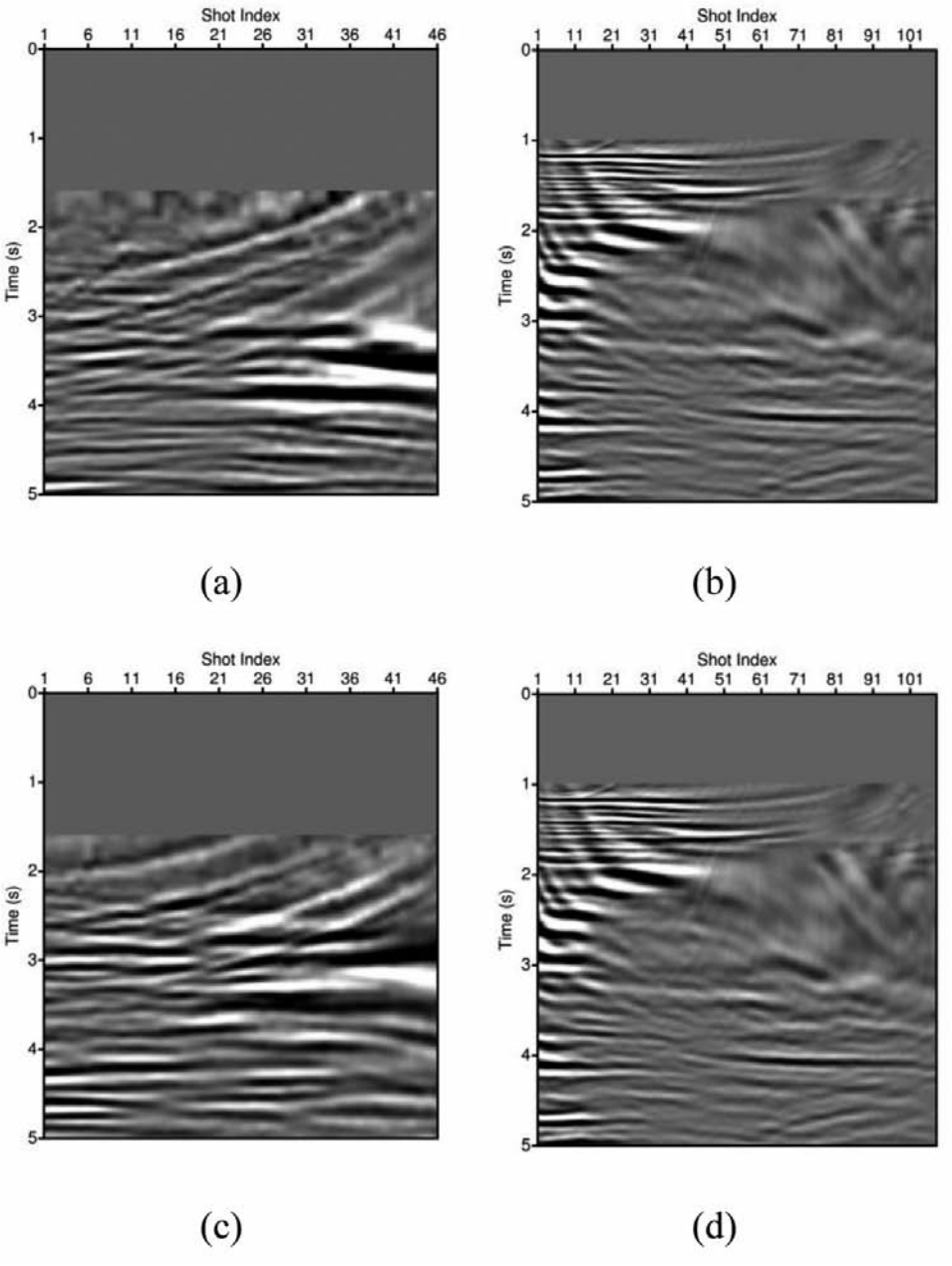

Fig. 18. Common image gathers from the previous migration images (Fig. 17). Panels (a) and (b) show common image gathers from the conventional inversion algorithm. Panels (c) and (d) show common image gathers from the inverted models that used the scaling method. The images in panels (a) and (c) were extracted 10 km from the left edge of the model, and the images in (b) and (d) were extracted 26 km from the left edge of the model.

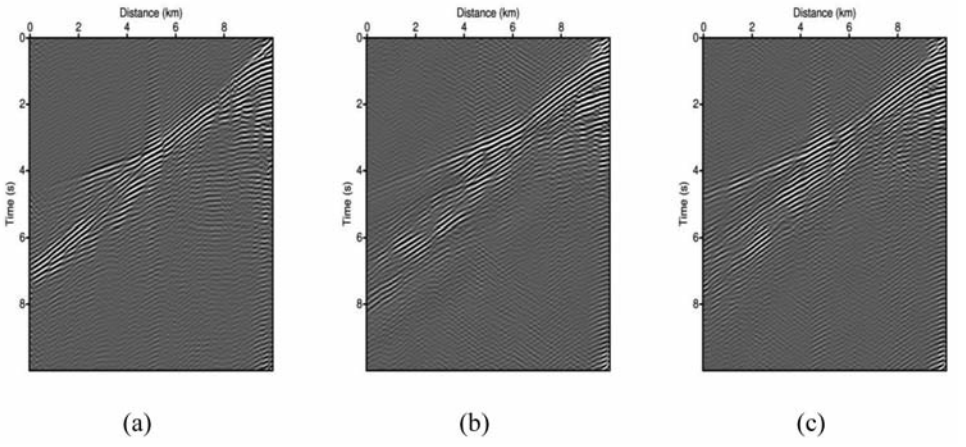

Fig. 19. Seismograms from (a) field data, (b) the inverted model using the conventional gradient, and (c) the inverted model using the scaled gradient.

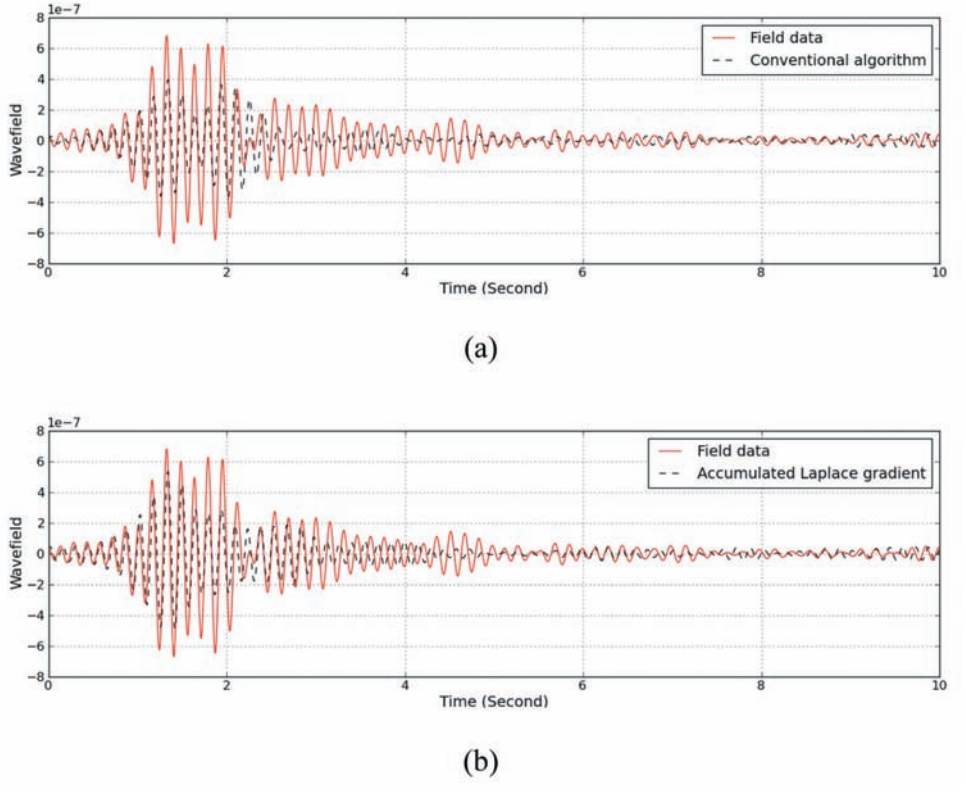

Fig. 20. Comparisons between field and synthetic time traces using (a) the conventional algorithm and (b) the gradient scaling algorithm at a 1.6 km offset.

CONCLUSIONS

In this study, we presented a gradient scaling method that uses an empirical approach to Laplace-domain waveform inversion in acoustic-elastic coupled media. The proposed gradient is computed by multiplying the conventional gradients by the accumulated gradients. The accumulated gradient is obtained from the accumulated sum of the squares of the conventional gradient with depth. We compared the conventional and scaled gradients using a synthetic salt model. Both inversions provided accurate long-wavelength results. However, the scaled gradient removed the numerical artifacts near the irregular interface and recovered high-velocity structures more accurately. We also tested each gradient using a field dataset. The scaled gradient emphasized the deep-water salt dome structure and attenuated artifacts near the irregular seafloor. The results of the frequency-domain inversions, reverse time migration images, common image gathers and synthetic seismograms indicated that the gradient scaling method could improve Laplace-domain inversion results. The scaling method that uses the accumulated gradient is designed to attenuate seafloor artifacts and to improve the recovery of deep-water high-velocity structures. This method can thus be applied to inverting marine seismic data that are acquired over high-velocity structures, such as salt diapers and basalts.

ACKNOWLEDGMENTS

This research was part of the project entitled 'Korea-Polar Ocean in Rapid Transition (KOPRI, PM15040)', which was funded by the Ministry of Oceans and Fisheries, Korea, and also received funding from the Korea Polar Research Institute (KOPRI, PE15050).

REFERENCES

Al-Yahya, K., 1989. Velocity analysis by iterative profile migration. Geophysics 54: 718-729.

Aminzadeh, F., Burkhard, N., Nicoletis, L., Rocca, F. and Wyatt, K., 1994. SEG/EAEG 3-D modeling project: 2nd update. The Leading Edge, 13: 949-952,

Bae, H.S., Shin, C., Cha, Y.H., Choi, Y. and Min, D.J., 2010. 2D acoustic-elastic coupled waveform inversion in the Laplace domain. Geophys. Prosp., 58: 997-1010.

Billette, F. and Lambaré, G., 1998. Velocity macro-model estimation from seismic reflection data by stereotomography. Geophys. J. Internat., 135: 671-690. doi: 10.1046/j.1365-246X.1998.00632.x

Biondi, B., 1990. Seismic velocity estimation by beam stack. Ph.D. Dissertation, Stanford University, Palo Alto, CA.

Biondi, B., 1992. Velocity estimation by beam stack. Geophysics, 57: 1034-1047.

Bishop, T.N., Bube, K.P., Cutler R.T., Love, P.L., Resnick, J.R., Shuey, R.T., Spindler, D.A. and Wyld, H.W., 1985. Tomographic determination of velocity and depth in laterally varying media. Geophysics, 50: 903-923.

Brenders, A.J. and Pratt, R.G., 2007. Full waveform tomography for lithospheric imaging: results from a blind test in a realistic crustal model. Geophys. J. Internat., 168: 133-151.

Brossier, R., Operto, S. and Virieux, J., 2009. Seismic imaging of complex onshore structures by 2D elastic frequency-domain full-waveform inversion. Geophysics, 74: WCC105-WCC118.

Bunks, C., Salek, F.M., Zaleski, S. and Chavent, G., 1995. Multiscale seismic waveform inversion. Geophysics, 60: 1457-1473. doi: 10.1190/1.1443880

Chiu, S.K.L. and Stewart, R.R., 1987. Tomographic determination of three-dimensional seismic velocity structure using well-logs vertical seismic profiles and surface seismic data. Geophysics, 52: 1085-1098.

Choi, Y., Min, D.-J. and Shin, C., 2008. Two-dimensional waveform inversion of multicomponent data in acoustic-elastic coupled media. Geophysics, 56: 863-881.

Chung, W., Shin, C. and Pyun, S., 2010. 2D elastic full waveform inversion in the Laplace domain. Bull. Seismol. Soc. Am., 100: 3239-3249.

Docherty, P., 1992. Solving for the thickness and velocity of the weathering layer using 2-D refraction tomography. Geophysics, 57: 1307-1318.

Docherty, P., Silva, R., Singh, S., Song, Z. and Wood, M., 1997. Migration velocity analysis using a genetic algorithm. Geophys. Prosp., 45: 865-878.

Farra, V. and Madariaga, R., 1988. Non-linear reflection tomography. Geophys. J. Internat., 95: 135-147.

Gauthier, O., Virieux, J. and Tarantola, A., 1986. Two-dimensional nonlinear inversion of seismic waveforms: numerical results. Geophysics, 51: 1387-1403.

Geller, R.J. and Hara, T., 1993. Two efficient algorithms for iterative linearized inversion of seismic waveform data. Geophys. J. Internat., 115: 699-710. doi: 10.1111/gji.1993.115.issue-3

Ha, W., Cha, Y.H. and Shin, C., 2010a. A comparison between Laplace domain and frequency domain methods for inverting seismic waveforms. Explor. Geophys., 41: 189-197. doi: 10.1071/EG09031

Ha, T., Chung, W. and Shin, C., 2009. Waveform inversion using a back-propagation algorithm and a Huber function. Geophysics, 74: R15-R24.

Ha, W., Pyun, S., Yoo, J. and Shin, C., 2010b. Acoustic full waveform inversion of synthetic land and marine data in the Laplace domain. Geophys. Prosp., 58: 1033-1047.

Ha, W. and Shin, C., 2012. Laplace-domain full-waveform inversion of seismic data lacking low frequency information. Geophysics, 77: 199-206.

Hampson, D. and Russell, B., 1984. First break interpretation using generalized linear inversion. J. Canad. Soc. Explor. Geophys., 20: 40-54.

Jin, S. and Madariaga, R., 1993. Background velocity inversion with a genetic algorithm. Geophysics, 20: 93-96.

Kang, S.G., Bae, H. and Shin, C., 2012. Laplace-Fourier domain waveform inversion for fluid-solid media. Pure Appl. Geophys., 169: 2165-2179.

Kim, M.H., Choi, Y., Cha, Y.H. and Shin, C., 2009. 2-D frequency-domain waveform inversion of coupled acoustic-elastic media with an irregular interface. Pure Appl. Geophys., 166: 1967-1985.

Kolb, P., Collino, F. and Lailly, P., 1986. Pre-stack inversion of a 1-D medium. Proc. IEEE, 74: 498-508.

Komatitsch, D., Barnes, C. and Tromp, J., 2000. Wave propagation near a fluid-solid interface: a spectral-element approach. Geophysics, 65: 623-631.

Lailly, P., 1983. The seismic inverse problem as a sequence of before stack migrations. Expanded Abstr., Conf. Inverse Scatt.: Theory Applicat. Mathemat.: 206-220.

Mora, P., 1987. Non-linear two-dimensional elastic inversion of multioffset seismic data. Geophysics, 52: 1211-1228.

Operto, S., Ravaut, C., Improta, L., Virieux, J., Herrero, A. and Dell'Aversana, P., 2004. Quantitative imaging of complex structures from multi-fold wide aperture seismic data: a case study. Geophys. Prosp., 52: 625-651. doi: 10.1111/gpr.2004.52.issue-6

Plessix, R.-E., 2009. 3D frequency-domain full-waveform inversion with an iterative solver. Geophysics, 74: WCC149-WCC157. doi: 10.1190/1.3211198

Pratt, R.G., Shin, C. and Hicks, G.J., 1998. Gauss-Newton and full Newton method in frequency domain seismic waveform inversion. Geophys. J. Internat., 133: 341-362.

Pyun, S., Son, W. and Shin, C., 2011. 3D acoustic waveform inversion in the Laplace domain using an iterative solver. Geophys. Prosp., 59: 386-399.

Qin, F., Cai, W. and Schuster, G.T., 1993. Inversion and imaging of refraction data. Expanded Abstr., 81st Ann. Internat. SEG Mtg., San Antonio, 12: 613-615. doi:10.1190/1.1822567

Riabinkin, L.A., 1957. Fundamentals of resolving power of controlled directional reception (CDR) of seismic waves. In: Slant Stack Processing. Geophysics Reprint Series, 1991, SEG, Vol. 14. Translated and paraphrased from Prikladnaya 16, 3-36.

Riabinkin, L.A., Napalkov, I.V., Znamenskii, V.V., Voskresenskii, I.N. and Rapoport, M., 1962. Theory and practice of the CDR seismic method. Transact. Gubkin Inst. Petrochem. Gas Product. (Moscow), 39.

Shin, C. and Cha, Y.H., 2008. Waveform inversion in the Laplace domain. Geophys. J. Internat., 173: 922-931.

Shin, C. and Ha, W., 2008. A comparison between the behavior of objective functions for waveform inversion in the frequency and Laplace domains. Geophysics, 73: VE119-VE133.

Shin, C., Jang, S. and Min, D., 2001. Improved amplitude preservation for prestack depth migration by inverse scattering theory. Geophys. Prosp., 49: 592-606.

Shin, C. and Min, D.J., 2006. Waveform inversion using a logarithmic wavefield. Geophysics, 71: R31-R42.

Shin, C., Pyun, S. and Bednar, J.B., 2007. Comparison of waveform inversion, part 1: conventional wavefield vs logarithmic wavefield. Geophys. Prosp., 55: 449-464.

Shipp, R.M. and Singh, S.C., 2002. Two-dimensional full wavefield inversion of wide-aperture marine seismic streamer data. Geophysi. J. Internat., 151: 325-344.

Shtivelman, V., 1996. Kinematic inversion of first arrivals of refracted waves-A combined approach. Geophysics, 61: 509-519.

Sirgue, L., Barkved, O.I., Van Gestel, J.P., Askim, O.J. and Kommedal, J.H., 2009. 3D Waveform inversion on Valhall Wideazimuth OBC. Extended Abstr., 71st EAGE Conf., Amsterdam: U038. http://www.earthdoc.org/detail.php?pubid=24070.

Sirgue, L. and Pratt, R.G., 2004. Efficient waveform inversion and imaging: a strategy for selecting temporal frequencies. Geophysics, 69: 231-248.

Stefani, J.P., 1995. Turing-ray tomography. Geophysics, 60: 1917-1929.

Symes, W., 2008. Migration velocity analysis and waveform inversion. Geophys. Prosp., 56: 765-790. doi: 10.1111/gpr.2008.56.issue-6

Symes, W. and Carazzone, J., 1991. Velocity inversion by differential semblance optimization. Geophysics, 56: 654-663.

Tarantola, A., 1984. Inversion of seismic reflection data in the acoustic approximation. Geophysics, 49: 1259-1266.

Vigh, D., Starr, W., Kapoor, J. and Li, H., 2010. 3D full waveform inversion on a Gulf of Mexico WAZ data set. Expanded Abstr., 80th Ann. Internat. SEG Mtg., Denver: 957-961.

Virieux, J. and Operto, S., 2009. An overview of full-waveform inversion in exploration geophysics. Geophysics, 74(6): WCC1-WCC26, doi: 10.1190/1.3238367.

White, D.J., 1989. Two-dimensional seismic refraction tomography. Geophys. J. Internat., 97: 223-245.

Zhang, J. and Toksöz, M.N., 1998. Nonlinear refraction traveltime tomography. Geophysics, 63: 1726-1737.

Zhu, X. and McMechan, G.A., 1989. Estimation of a two-dimensional seismic compressional-wave velocity distribution by iterative tomographic imaging. Internat. J. Imaging Syst. Technol., 1: 13-17.

Zienkiewicz, O.C., Taylor, R.L. and Zhu, J.Z., 2005. The Finite Element Method: Its Basis and Fundamentals. Butterworth-Heinemann, Oxford.